Chemical Geology 508 (2019) 197–209

Contents lists available at ScienceDirect

Chemical Geology

journal homepage: www.elsevier.com/locate/chemgeo

Multiphase inclusions in peritectic garnet from granulites of the Athabasca granulite terrane (Canada): Evidence of carbon recycling during Neoarchean crustal melting

Tommaso Tacchetto[a,*], Omar Bartoli[a], Bernardo Cesare[a], Márta Berkesi[b], László Előd Aradi[b], Gregory Dumond[c], Csaba Szabó[b]

[a] Dipartimento di Geoscienze, Università di Padova, Via Gradenigo 6, 35131 Padova, Italy
[b] Lithosphere Fluid Research Lab, Institute of Geography and Earth Sciences, Eötvös University Budapest (ELTE), Pázmány P. stny. 1/C, H-1117 Budapest, Hungary
[c] Department of Geosciences, University of Arkansas, Fayetteville, AR 72701, USA

ARTICLE INFO

Keywords:
Neoarchean crustal anatexis
Peritectic garnet
CO_2 fluid inclusions
Nanogranitoid
Melt/fluid immiscibility
FIB-SEM serial sectioning

ABSTRACT

In the last decade, the study of fluid and melt inclusions in partially melted rocks has become a key tool to acquire unprecedented information about crustal anatectic processes. In this study we report the results of the microstructural and microchemical investigation on multiphase inclusions trapped within peritectic garnet of a Neoarchean felsic granulite from the Upper Deck domain of the Athabasca granulite terrane, Canada. Inclusions have been studied by SEM-EDS, FIB-SEM serial sectioning and Raman microspectroscopy, and classified in terms of size and hosted phases. Type I multiphase inclusions are small (≤15 μm), primary in origin, and do not show evidence of decrepitation. Their multiphase assemblage is made of ferroan magnesite, quartz and graphite in association with minor amounts of corundum, pyrophyllite and Zn-spinel. Calcite, dolomite and zinc-bearing sulphide may also be present. The coexistence of quartz and corundum in these inclusions is interpreted as the product of metastable growth within pores of extremely small size. The fluid phase of Type I inclusions, always present in amounts > 40 vol%, is CO_2-rich (96.5 mol%) with traces of N_2 (3.3 mol%) and CH_4 (0.2 mol%). These carbon-rich Type I inclusions coexist in the same cluster with primary melt inclusions (nanogranitoids; Type II). These are large (up to 50 μm) and composed of K-feldspar, quartz and plagioclase with minor amounts of graphite, biotite and aluminosilicate. Because nanogranitoids are droplets of anatectic silicate melt formed and trapped during incongruent melting of crustal rocks, the coexistence of Type I multiphase inclusions proves the presence of a carbon-rich fluid during the Neoarchean anatexis (800–950 °C, 0.6–1.4 GPa) of this portion of continental crust, in a likely situation of melt/fluid immiscibility. According to phase equilibria modelling, the uncommon multiphase assemblage within Type I inclusions is here interpreted as the result of a post-entrapment carbonation reaction between an original CO_2-bearing fluid and the garnet host during rock cooling from UHT conditions.

1. Introduction

The Neoarchean Era (2.8–2.5 Ga) represents a fundamental stage in the geological evolution of our planet (Brown, 2006, 2007; Laurent et al., 2014; Farina et al., 2015; Spencer et al., 2017). The contemporaneous appearance of two contrasting types of metamorphism in the Neoarchean, the ultra-high temperature (UHT) and eclogite high-pressure (EHP) granulite metamorphism, is considered to record subduction-to-collision orogenesis and, therefore, the onset of plate tectonics (Brown, 2006). In particular, the UHT granulite metamorphic belts would have developed in settings analogous to modern continental backarcs (Brown, 2007; Dumond et al., 2017).

Since the time continental crust has existed, it has geochemically evolved over geological time towards a more felsic and incompatible element-enriched upper part and a more residual lower crust (i.e., the geochemical differentiation or intracrustal reworking) by a combination of processes such as HT-UHT metamorphism, anatexis and migration of melts towards upper crustal levels (Sawyer et al., 2011). Furthermore, melting processes have not only modified the composition of the continental crust, but they have also altered its rheological properties (Jamieson et al., 2011). Fluids and melts present during high-temperature metamorphism and anatexis have played a fundamental

* Corresponding author.
E-mail address: tommaso.tacchetto@unipd.it (T. Tacchetto).

https://doi.org/10.1016/j.chemgeo.2018.05.043
Received 9 December 2017; Received in revised form 9 May 2018; Accepted 30 May 2018
Available online 04 June 2018

role in mass and heat transfers (Newton, 1980; Touret and Dietvorst, 1983; Santosh et al., 2008; Brown, 2013; Weinberg and Hasalová, 2015). However, the evidence of the former fluids and melts has often been erased by slow cooling and recrystallization of high-grade metamorphic rocks, preventing the detailed characterization of fluid-melt-rock interactions during crustal anatexis.

During the last decade, the microstructural and microchemical study of primary anatectic melt inclusions in peritectic minerals from high-grade anatectic rocks (nanogranitoids; Cesare et al., 2015; Bartoli et al., 2016) has been demonstrated as an innovative approach to investigate the processes of crustal melting and granitoid magma evolution (Cesare et al., 2009; Ferrero et al., 2012; Bartoli et al., 2013a, 2016). In fact, peritectic phases formed by incongruent melting of crustal protoliths can entrap small portions of coexisting anatectic melt (Cesare et al., 2009, 2015), giving us access to the natural anatectic melt composition (Acosta-Vigil et al., 2010, 2007; Bartoli et al., 2013b, 2014). The widespread occurrence of CO_2-rich fluid inclusions in granulitic terranes (often mixed with small quantities of CH_4 and N_2) have already witnessed the possible role of low-a_{H2O} fluids during high-grade metamorphism (Touret and Dietvorst, 1983; Hollister, 1988; Frezzotti and Touret, 2014). Moreover, the recent findings of droplets of carbonatitic melt of crustal origin (nanocarbonatites) or of CO_2-bearing fluid inclusions, both of which coexist with nanogranitoids, have opened up new possibilities to investigate fluid-melt-rock interactions during high-temperature metamorphism and crustal melting (Ferrero et al., 2014, 2016b).

In this contribution, we report the occurrence of primary carbon-rich multiphase inclusions trapped in the peritectic garnets of the Upper Deck domain (Athabasca granulite terrane, Canada). These rocks underwent partial melting during Neoarchean (2.61–2.55 Ga) UHT-HP metamorphism (> 800 °C and 0.6–1.4 GPa), as the consequence of crustal thickening, burial and coeval emplacement of MORB-like mafic sills (Snoeyenbos et al., 1995; Baldwin et al., 2006; Dumond et al., 2015, 2017). The uncommon daughter minerals assemblage within multiphase inclusions, represents a novel report in the fluid and melt inclusions literature. The application of modern cutting edge techniques has permitted detailed microstructural and microchemical constraints on the nature of these multiphase inclusions, leading to a better understanding of the melting processes of this portion of the deep Archean crust.

2. Geological setting

The Athabasca granulite terrane represents a large region (> 20.000 km^2) of continental lower crust exposed north of the Athabasca basin, in the northern region of Saskatchewan, Canada (Dumond et al., 2008; Mahan et al., 2008) (Fig. S1). The region is composed of Archean to Paleoproterozoic mafic and felsic granulites, orthogneisses, paragneisses and minor eclogites (Mahan et al., 2003, 2006; Mahan and Williams, 2005). The most studied portion is the East Athabasca mylonite triangle (EAmt; Hanmer, 1994, 1997). The EAmt is divided into three lithotectonic domains: Chipman, Upper Deck and Northwestern (Hanmer et al., 1994; Williams and Hanmer, 2006; Williams et al., 2009; Mahan et al., 2011). All three domains consist of Middle to Late Archean (ca. 3.2 to 2.6 Ga) igneous protoliths strongly reworked during Neoarchean high-pressure metamorphism (culminating at ca. 2.55–2.54 Ga; Dumond et al., 2015) and in the Paleoproterozoic at ca. 1.9 Ga (Hanmer et al., 1994; Snoeyenbos et al., 1995; Hanmer et al., 1995a, 1995b; Kopf, 1999; Williams et al., 2000; Baldwin et al., 2003, 2004; Williams and Hanmer, 2006; Baldwin et al., 2006; Mahan et al., 2006; Flowers et al., 2006; Dumond et al., 2008, 2010, 2015).

The rocks with the highest metamorphic grade in the Athabasca granulite terrane crop out in the Upper Deck domain, a ca. 10 km-thick succession of garnet-rich felsic granulites, garnetites and paragneisses that are interlayered with mafic sills occurring as granulites and minor eclogites (Hanmer et al., 1994; Snoeyenbos et al., 1995; Hanmer, 1997; Baldwin et al., 2003, 2004, 2006, 2007; Baldwin et al., 2015; Dumond et al., 2015, 2017).

Felsic granulites are the most common lithology of the Upper Deck domain, and mostly consist of quartzo-feldspathic mylonitc gneisses with abundant red-brownish garnets (Snoeyenbos et al., 1995). These rocks are considered as the residual product of biotite breakdown-melting of metasedimentary protoliths at UHT conditions (950 °C) during prograde burial that occurred between 2.61 and 2.55 Ga (Baldwin et al., 2006; Dumond et al., 2015). The HT metamorphism and partial melting initiated during Neoarchean intraplating of MORB-like basalts, which were derived from decompression melting of fertile lherzolite during continental extension and back-arc basin formation (Dumond et al., 2017). The subsequent tectonic contraction and prograde crustal thickening, resulted in the closure and burial of the hot back-arc basin, providing peak metamorphic conditions exceeding 950 °C and ≥ 1.4 GPa, culminating at 2.58–2.52 Ga (Snoeyenbos et al., 1995; Baldwin et al., 2003, 2006; Dumond et al., 2015, 2017). Exhumation and cooling of the terrain occurred between 1.9 and 1.7 Ga after a period of re-heating and crustal reactivation during dextral transpression at ca. 1.92–1.90 Ga, as consequence of arc-continent collision (Dumond et al., 2008, 2010; Regan et al., 2014).

3. Analytical techniques

Thin and thick sections (30 μm to 120 μm) were prepared to investigate the multiphase inclusions and the host garnet. Preliminary petrographic observations using optical microscope in transmitted light were conducted at the Dipartimento di Geoscienze, University of Padova. Back-scattered (BSE) and secondary electron (SE) imaging, and Energy Dispersive Spectrometry (EDS) qualitative analyses on opened inclusions, along with elemental X-ray maps, were acquired using two types of scanning electron microscope (SEM): 1) CAM SCAN MX3000, equipped with LaB_6 cathode, at the Dipartimento di Geoscienze, University of Padova; and 2) AMRAY 1830 I/T6, equipped with W cathode, at the Department of Petrology and Geochemistry, Eötvös Loránd University at Budapest, Hungary. Both BSE and SE images were acquired using 20 kV accelerating voltage at different magnifications. Elemental X-ray maps of the host garnet were acquired using 25 kV accelerating voltage with resolution of 512 × 400 and 1024 × 800 pixels. Major element composition of the host garnet was obtained using a CAMECA SX50 electron microprobe (EMP) of C.N.R., Instituto di Geoscienze e Georisorse, Sezione di Padova. Analyses were performed along transects across the grains using an accelerating voltage of 15 kV and sample current of 15 nA. The chemical composition of re-homogenized melt inclusions was determined using the Jeol JXA 8200 Superprobe at the Dipartimento di Scienze della Terra, Università di Milano, and using a 15 kV accelerating voltage, 5 nA beam current and 10 s on the peak and 5 s on background. Both the solid and fluid phases within the investigated inclusions were analysed at the Faculty of Science Research and Instrument Core Facility of Eötvös University, Budapest (ELTE FS-RICF) using a HORIBA LabRam HR (high resolution) Raman microspectrometer. A frequency-doubled Nd:YAG laser with 532 nm excitation wavelength was used. An OLYMPUS 100 × objective was adopted to focus the laser on the selected inclusions. Raman spectra of exposed solid phases were collected with an acquisition time 10–15 s for each spectrum, and 3 accumulations. Raman maps of ten different inclusions below the host surface were performed. Spectra were acquired between the spectral range of 100 and 1800 cm^{-1} and 2700 to 3800 cm^{-1} using a 50 μm confocal hole, 600 grooves/mm optical gratings, 2–3 × accumulations and 12 s acquisition time. The spectral resolution of measurements varied depending on the analytical parameters but was ≤ 7 cm^{-1}.

To identify the presence of H_2O, Raman spectra of eight different inclusions were collected at room temperature, then at +75 °C, +125 °C and + 200 °C using a Linkam THMS600 heating/cooling stage

(see details in Berkesi et al., 2009). Data were collected in the region between 1120 and 1570 cm^{-1} and from 3560 to 3730 cm^{-1}, using a 100 µm confocal hole, 1800 grooves/mm, 5–6× accumulations and 60–200 s acquisition time. To avoid fluorescence emissions a laser with 633 nm excitation wavelength was used.

Raman data were processed using LabSpec v5.41.15 and Omnic for Dispersive Raman software. The online database Ruff project published by Lafuente et al. (2015) and the online database of the Laboratoire de Géologie de Lyon were used to identify the solid phases.

Selected inclusions, located from 3 to 8 µm below the garnet surface, were analysed by serial sectioning using a FEI QUANTA 3D focused ion beam-scanning electron microscopy (FIB-SEM) technique at the ELTE FS-RICF, Budapest, Hungary. Analyses were conducted using a 15 kV accelerating voltage and 23.7–190 pA current, depending on the inclusion size and magnification. For FIB-SEM analyses the pre-selected area was covered by a thin platinum layer (ca. 2 µm) in order to make the surface of the sample more resistant to the mechanical abrasion by the Ga^+ ion beam and to prevent the formation of fractures and imperfections on the cutting surface. Utilizing a high current Ga^+ ion beam, three trenches were milled around the selected inclusions. By using the low current ion beam, the FIB-SEM technique permits removal of thin foils (ca. 250 nm in this study) of material gradually exposing new portions of the selected inclusion and avoiding the loss of material that usually occurs during conventional sample preparation. FIB-SEM serial sectioning obtains a precise representation of the inclusion and allows us to calculate the volume proportion of each phase. The stepwise exposure of ca. 250 nm was decided on the basis of the average size of inclusions and the hosted solid phases. Imaging of the exposed surface was performed under both BSE and SE mode. Solid phases were analysed and identified using EDS spectra, BSE and SE images, together with previously-obtained Raman maps. 3D reconstructions were made using Amira 5.2.2 software and Reconstruct software.

4. Sample petrography

The felsic granulite of the Upper Deck domain appears as a fine grained migmatitic paragneiss mainly composed of quartz and ternary feldspar in association with garnet, sillimanite, kyanite, minor plagioclase and rare biotite (Fig. 1). Accessory phases are rutile, graphite, zircon, monazite and apatite. The main sub-horizontal foliation (S_1) is defined by ribbons of elongate quartz and feldspars, blades of sillimanite and kyanite along with garnet aggregates (Fig. 2a, b). A sub-vertical S_2 foliation, locally determined by fractured garnets filled by kyanite, sillimanite, quartz and rutile can also be present (Dumond et al., 2015). Garnet is ubiquitous and occurs as 0.5–1.5 mm porphyroblasts representing ca. 25–30 vol% of the modal volume of the rock (Fig. 2a, b). It is subhedral and contains abundant mineral inclusions. Rounded quartz represents the most common inclusion with crystals up to 100 µm in size. Other inclusions are rutile needles, sillimanite, kyanite, monazite, apatite, zircon, and less frequent graphite and biotite. Kyanite and sillimanite occur both in the matrix (≤1 vol%) and as inclusions in garnet porphyroblasts. As already observed by Dumond et al. (2015), prismatic sillimanite is preferentially located at the core of the host garnet whereas euhedral kyanite is included at its rim. This has been interpreted as the consequence of variations in P-T conditions during garnet growth. In the matrix, sillimanite is anhedral, deformed and fractured, always adjacent to garnet (Fig. 2c, d). Biotite (up to 200 µm in size) is rare and may be present as inclusion in garnet characterized by a high Ti-content (> 5.4 wt%) (Fig. 2e). Elongated graphite (3–5 vol%) is widespread in the rock (Fig. 2f). Rutile is an abundant accessory phase (2–3 vol%), occurring as rounded grains in the matrix (ca. 150 µm) and as oriented needles up to hundreds of micrometers in length in garnet (Fig. 2g). Other accessory phases are apatite, monazite and zircon. Feldspars are mostly ternary and characterized by anti-perthite microstructure (Fig. 2h); together with quartz they form the matrix of the rock. Symplectic intergrowths of quartz and plagioclase can be present (Fig. 2i). Lobate-cuspate grains and films of K-feldspar are visible among quartz grains (Fig. 3a, b).

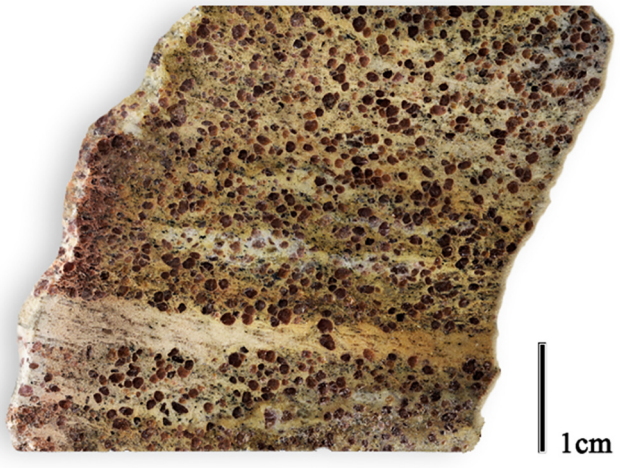

Fig. 1. The investigated rock sample from the Upper Deck domain. The main S_1 foliation is highlighted by the alternations of white leucocratic layers and bands rich in millimetre-sized red-brownish garnet crystals.

5. Characterization of the multiphase inclusions

5.1. Petrography of the inclusions

Garnets of the felsic granulite enclose sub-circular clusters of dark inclusions occurring exclusively in the cores (Fig. 4a). These inclusions are generally ≤10–15 µm in size (with some exception up to 50 µm) and characterized by negative crystal to sub-spherical shape (Fig. 4b). Evidence of decrepitation (i.e., halos around the inclusions), as post entrapment processes leading to partial fluid loss, is uncommon. Rather, the inclusions show undisturbed features (Fig. 4b). The distribution of inclusions (Roedder, 1984) along crystal growth zone strongly supports their primary origin, i.e., that they have been trapped during the garnet growth. Inclusions appear mostly opaque under the plane-polarized light and are observed at variable depth within the garnet (Fig. 4b). Observation of inclusions under crossed polarized light and high magnification shows that inclusions contain polycrystalline aggregates of birefringent crystals (Fig. 4c). Because of the low transparency and the small size, neither the presence of bubbles nor optical properties of crystal phases within the inclusions are recognisable by optical microscopy alone. Secondary inclusions are also present in the garnets. They are distributed in planar arrays along healed fractures that crosscut the host growth surface boundaries. However, as they have been formed after garnet formation and under conditions that may differ from those of anatexis, they are not considered further in this study.

5.2. SEM-EDS analysis

SEM-EDS observations permitted identification of two different types of inclusions coexisting in the same cluster and differing in terms of size and constituent phases (Fig. 4d). Type I inclusions (Fig. 5a–c) are smaller (4–15 µm) and represent the largest fraction of the clusters (80–90 vol%). They are polycrystalline, with mineral sizes generally ≤6 µm, and mainly composed of quartz, Fe-Mg-Ca carbonates, corundum and graphite. A Zn-Al phase (possibly a Zn-spinel) has been occasionally detected. Type II inclusions are generally larger (up to 50 µm; Fig. 4d), but much less common than Type I (10–20 vol%). They are totally crystallized, and composed of quartz, plagioclase, K-

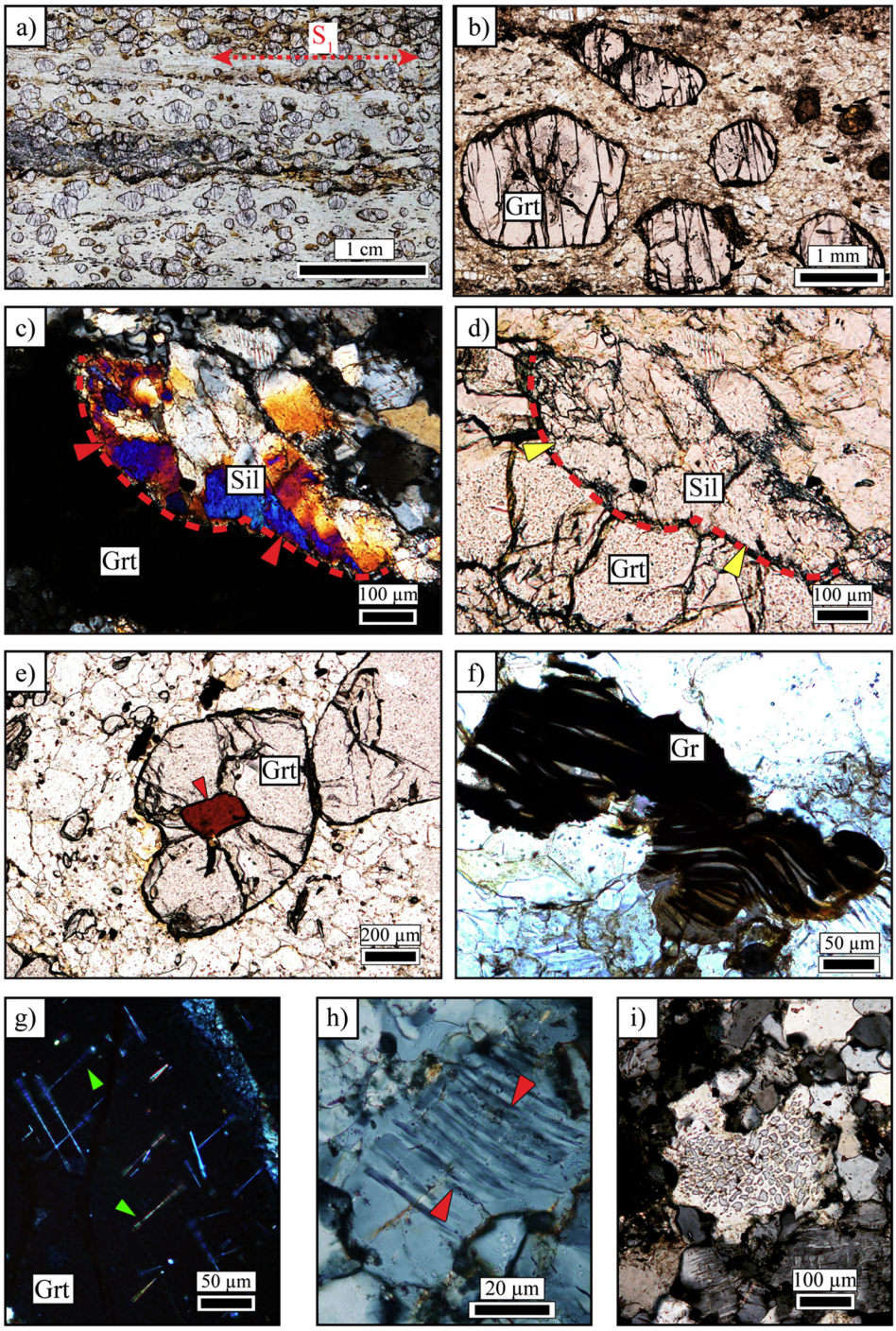

Fig. 2. Photomicrographs showing the characteristic petrographic features of the felsic granulites. Mineral abbreviations after Kretz (1983). a) The main sub-horizontal S_1 foliation of the rock defined by ribbons of quartz and feldspars along with garnet porphyroblasts; b) anhedral to subhedral garnets surrounded by ribbons of quartz and feldspars; c–d) resorbed garnet replaced by sillimanite (red and yellow arrows); e) subhedral biotite (red arrow) included in garnet; f) graphite crystals; g) oriented rutile needles (green arrows) enclosed in garnet; h) alkali feldspar characterized by anti-perthitic microstructure (red arrows); i) symplectic intergrowth of quartz and plagioclase. (For interpretation of the references to colour in this figure legend, the reader is referred to the web version of this article.)

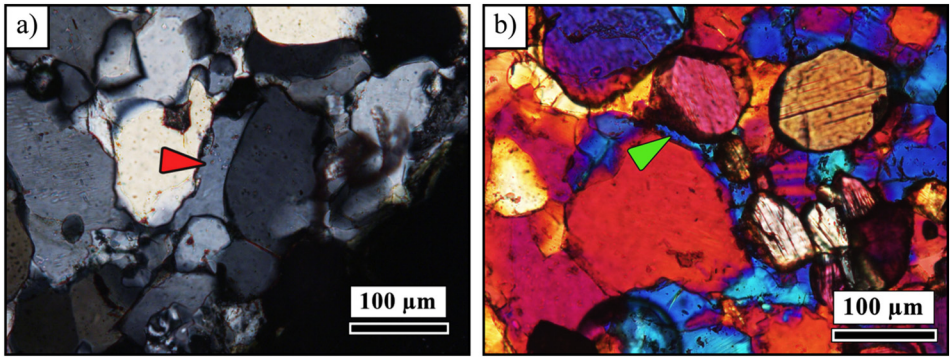

Fig. 3. a–b) Photomicrographs showing the characteristics microstructures of melt films and pools (red and green arrows). Lobate-cuspate grains and films of K-feldspar crystallized between quartz grains; a) crossed-polarized light; b) crossed polarizers with λ plate. (For interpretation of the references to colour in this figure legend, the reader is referred to the web version of this article.)

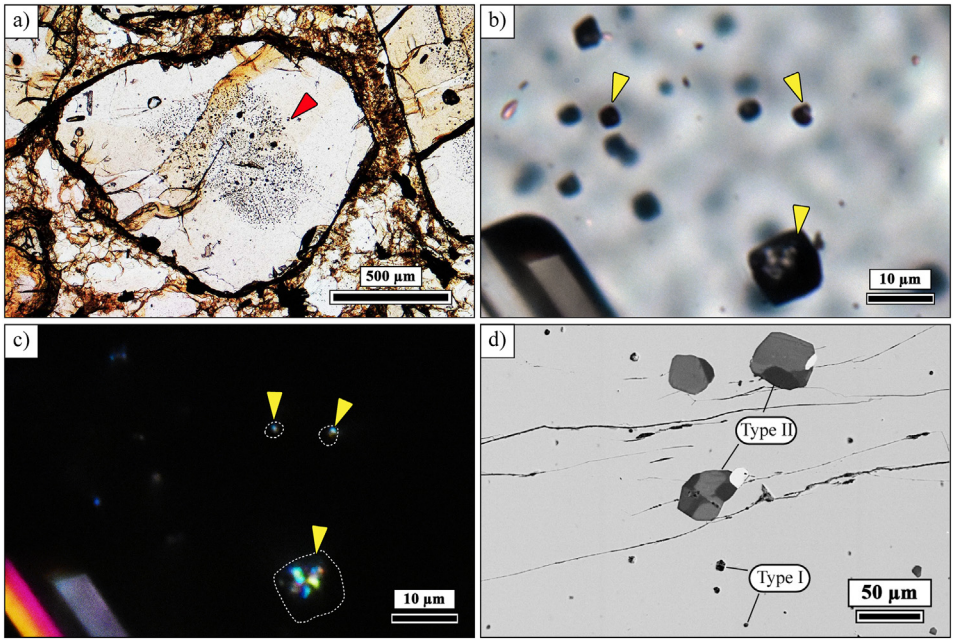

Fig. 4. a) Sub-circular cluster (red arrow) of multiphase inclusions in zonal arrangement at the core of garnet; (b, c) photomicrographs of multiphase Type I (yellow arrows) inclusions in garnet (plane-polarized and crossed-polarized light, respectively). In (c) the presence of aggregates of birefringent crystals within the inclusions is shown; (d) BSE image of Type I and II multiphase inclusions at the garnet core. (For interpretation of the references to colour in this figure legend, the reader is referred to the web version of this article.)

feldspar ± biotite and ± Al-silicate (Fig. 5d–i). Rutile and graphite are common as accessory phases; sometimes zircon and apatite have been observed. Fractures are often seen projecting from the inclusion into the host (Fig. 5d). The size of the daughter minerals depends on the dimension of the inclusion but generally K-feldspar represents the largest phase (≤20 µm). The latter is subhedral and often characterized by exsolution lamellae of plagioclase (Fig. 5i). Euhedral to subhedral crystals of biotite have been observed (Fig. 5g) and they are likely to be the first phases to have crystallized in Type II inclusions (see Ferrero et al., 2012). Plagioclase and quartz are usually interstitial. Lobate boundaries among minerals suggest intergrowth microstructures formed from simultaneous crystallization of a trapped melt (Cesare et al., 2011; Ferrero et al., 2012).

5.3. Raman microspectroscopy analysis

It was observed that after sample preparation and polishing, most of Type I inclusions were partially or completely empty. This evidence suggested not only that part or all of the solid phases contained in were lost by mechanical removal, but also the possible presence of a fluid phase, which was removed during inclusion opening and exposure on the garnet surface. Therefore, in order to identify all the phases, additional non-destructive Raman analysis and mapping were performed on exposed and unexposed Type I inclusions (i.e., with undisturbed petrographic features). The latter are supposed to preserve the entrapped fluid phase, assuming no partial fluid loss occurred after the entrapment.

Carbonates within Type I inclusions consist mainly of a solid solution between siderite and magnesite that can be classified as ferroan magnesite (Fig. 6a). Corundum (bands at 749, 416 and 377 cm^{-1}), calcite (bands at 1084, 708 and 271 cm^{-1}) and dolomite (bands at 1095, 724 and 293 cm^{-1}) are sometimes present.

The spectra of graphite are characterized by a well-developed "disordered" band centred at 1345 cm^{-1} (Fig. 6b), suggesting a low degree of crystallinity (Wopenka and Pasteris, 1993; Cesare and Maineri, 1999).

Raman analyses of unexposed Type I inclusions also showed the systematic presence of a CO_2-rich fluid on the basis of the bands appearing at 1385 and 1280 cm^{-1} (Fig. 6c). The CO_2 density was calculated according to the method based on the distance (Δ) between the Fermi diad (two highest intensity Raman bands, see Wang et al., 2011). Results are reported in Table 1. Density values range between 0.5 and 0.7 g/cm^3. A higher density (ca. 0.9 g/cm^3) has been measured in one inclusion containing only CO_2. In addition, Raman analyses show the presence of two distinct peaks at 2326 cm^{-1} and at 2912 cm^{-1} (Fig. 6c), which are characteristic respectively of N_2 and CH_4 (Frezzotti et al., 2012b; Berkesi et al., 2017 and references therein). The nitrogen contribution from air was excluded by acquiring a Raman spectrum pointing the laser outside the inclusion on the host surface (Berkesi et al., 2017). The relative amounts of components in the fluid within Type I inclusions, calculated using the integrated band area proposed by Dubessy et al. (1989), are 96.5 mol% CO_2, 3.3 mol% N_2 and ca. 0.2 mol% CH_4.

Raman spectral imaging was performed on nine additional Type I inclusions (Fig. 7) occurring inside the cluster (i.e., they are primary inclusions). Detected solid phases were the same as those identified in the exposed inclusions, i.e., ferroan magnesite, quartz and graphite (Fig. 7; Fig. S2). In addition, pyrophyllite was found in some inclusions, identified based on peaks at 704, 349, 259 and 192 cm^{-1} (Figs. 6d, 7; Fig. S2). Raman microspectroscopy at temperatures of 75, 125 and 200 °C was carried out to search for small amounts of H_2O within Type I inclusions (Berkesi et al., 2009; Lamadrid et al., 2014). However, no traces of H_2O were observed.

5.4. FIB-SEM serial sectioning

The application of this sophisticated technique has offered the possibility to analyse sub-micron areas and to reconstruct the 3D distribution of phases within inclusions.

FIB-SEM serial sectioning has been performed on eight Type I inclusions, on which previous Raman spectral imaging was also carried out. Minerals were thus identified based on Raman and EDS spectra together with BSE-SE images.

The polycrystalline assemblage is always composed of ferroan magnesite, quartz and graphite (Figs. 8, 9). Crystals vary from subhedral to euhedral in shape, and occur in aggregates. Ferroan magnesite and quartz are the larger phases with a size range between 2 and 6 µm (Fig. 8). The different brightness on the BSE image of magnesite is related to its compositional zoning. As shown by SEM-EDS analyses, these lighter portions are characterized by lower Mg content (Fig. 8a). Graphite is smaller, generally as hundreds nanometers thin lamellae, and interstitial among other phases (Fig. 8b). It also occurs as subhedral

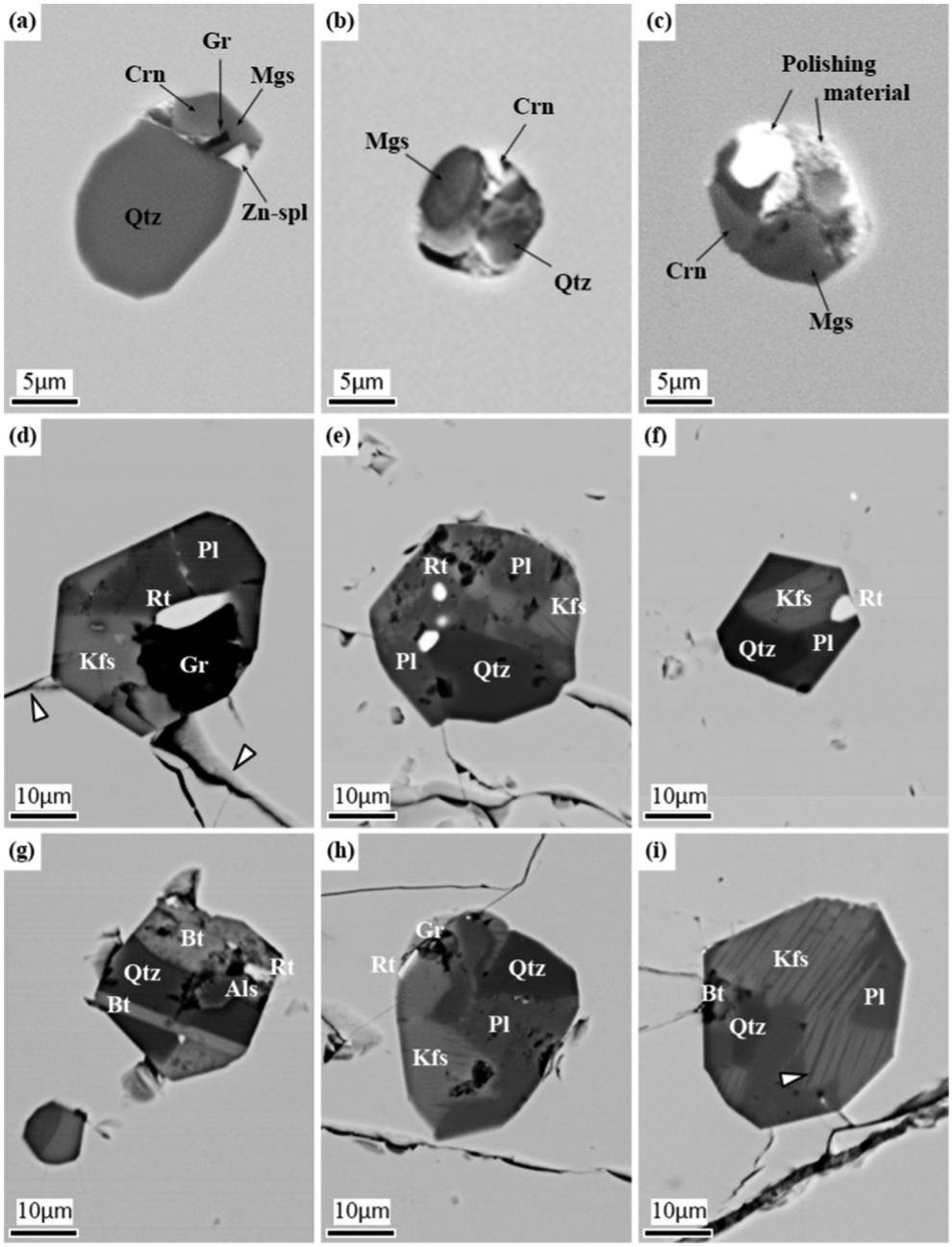

Fig. 5. BSE images of multiphase inclusions in garnet. (a), (b) and (c) Type I multiphase inclusions with the typical phase assemblage (ferroan magnesite, quartz, graphite, corundum and Zn-spinel). In (c) the top-right empty portion of the inclusion is filled with polishing material. (d), (e), (f), (g), (h) and (i) Type II inclusions. (d) Type II inclusion with negative crystal shape. White arrow: fractures projecting into the host; (f) Type II inclusion with well-developed negative crystal shape; (g) Type II inclusion with euhedral biotite and Al-silicate crystals; (i) Type II inclusion with isometric shape. White arrow: exsolution lamellae of plagioclase in K-feldspar.

crystal within magnesite (Fig. 8a). Subhedral crystals of corundum (up to ca. 3 μm) were found coexisting in contact with quartz (Figs. 8c, 9). Zn-spinel (ca. 500 nm in size) is always present while crystals of ca. 200 nm of a S-Zn bearing phase, probably a Zn sulphide, is sometimes detected. Pyrophyllite is observed as ca. 5 μm euhedral crystal crossing the inclusion cavity (Fig. 8a). An unidentified solid, named "Fe-bearing phase" has been observed in some cases. Its EDS spectrum is very similar to the host garnet but with higher Fe content (Fig. 8c). Combining the SEM images of all the slices, the 3D reconstruction of the investigated inclusions was obtained (Fig. 10). This procedure allows the calculation of both the volume of the inclusion cavity and of each single daughter phases. In Table 2, the volume percentage of the minerals, normalized to the total amount of solid phases detected in each inclusion, are reported. The vol% of the ferroan magnesite ranges from ca. 60 to 80%, that of quartz from ca. 10 to 25%, whereas the volume of graphite remains < 6.5%. Zn-spinel showed values up to 6% and corundum ranges between 4 and 10%.

FIB-SEM imaging together with the 3D reconstruction demonstrated the high fluid-filled porosity of Type I inclusions (Fig. 10d; Table 2), demonstrating that the non-crystalline portions of the cavity were filled with the fluid phase detected by micro-Raman analysis (Fig. 6c).

6. Chemical characterization of the host garnet

Garnet of felsic granulite is compositionally zoned and it is almandine rich ($Alm_{61-64}Sps_1Grs_{4-9}Prp_{30-33}$) with an X_{Mg} of 0.32–0.35. The results of X-ray elemental analyses and EMP measurements show an evident zoning of calcium (Figs. 11, S3; Table S1): a large low-Ca core and a high-Ca internal annulus are distinguishable. At the very rim, the calcium concentration decreases. Calcium concentration varies from ca. 1.5 wt% at the core up to ca. 3.5 wt% in the internal annulus. The external rim shows a Ca concentration < 2 wt%, similar to that of the garnet core (Table S1). Almandine and pyrope decrease in proximity of the high-grossular rim (Fig. S3). There is no microstructural

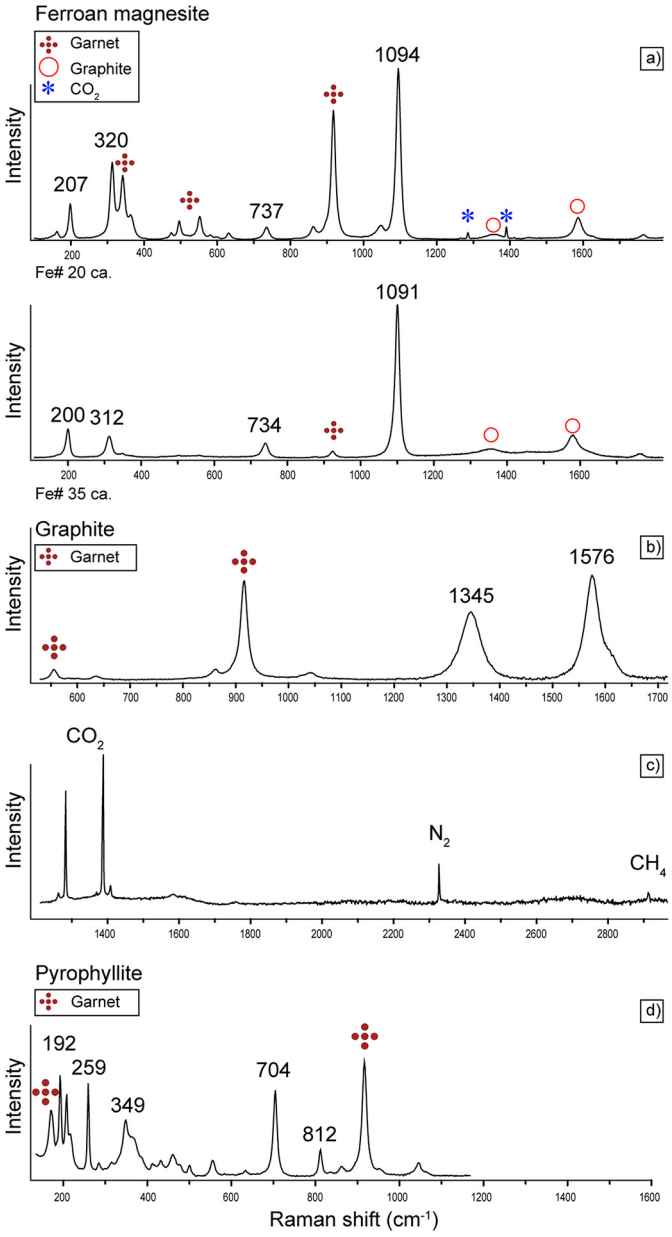

Fig. 6. Representative Raman spectra of phases of interest in multiphase inclusions Type I. (a) Ferroan magnesite with various Fe content. Note that peaks in the region between 100 and 300 cm^{-1} shifts towards lower wavenumbers with increasing in Fe# = [100 ∗ Fe/(Fe + Mg + Mn + Ca + Al)] according to the method proposed by Boulard et al. (2011); (b) graphite; (c) fluid components such as CO_2 (bands at 1385 and 1280 cm^{-1}), N_2 (bands at 2326 cm_1) and CH_4 (bands at 2912 cm^{-1}) detected in inclusions; (d) pyrophyllite. Numbers indicate the Raman band position of the respective phases.

relationship between the garnet zoning and the occurrence of multiphase inclusions (Fig. S3); in fact, inclusion clusters are mainly located in the garnet core but also extend into the high-Ca annulus.

7. Discussion

The felsic granulites of the Upper Deck domain represent the highest metamorphic grade recorded in the Athabasca granulite terrane. Despite the deformation and high temperature annealing, there is some clear textural evidence of the former presence of anatectic melt (see criteria in Holness and Sawyer, 2008; Holness et al., 2011; Cesare et al., 2011). This is observed both in the rock matrix, such as mineral

Table 1
Calculated CO_2 density (ρ) of inclusions studied by Raman maps. Calculation of the CO_2 density is based on the method described by Wang et al. (2011). Upper and Lower band refers to both the positions of the Fermi diad. Δ Fermi diad corresponds to the difference in peak position of the Fermi diad.

Inclusion	Upper band (ν-$2\nu_2$)	Lower band (ν-$2\nu_2$)	Δ Fermi diad	ρ_{calc} (g/cm^3)
1	1280.9	1385.0	104.13	0.6
2	1282.4	1386.4	103.95	0.5
3	1282.6	1386.7	104.14	0.6
4	1281.7	1386.1	104.31	0.7
5	1282.6	1386.6	104.01	0.5
8	1282.5	1386.6	104.09	0.6

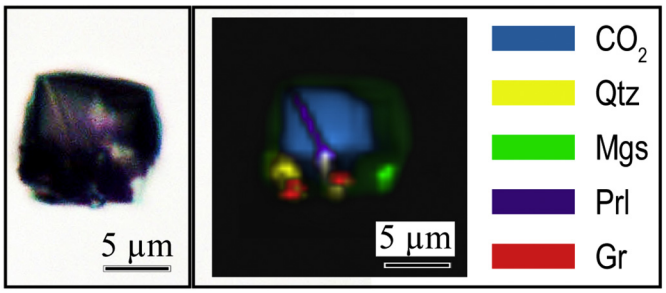

Fig. 7. Raman map of an unexposed multiphase Type I inclusion; (left) photomicrograph of the selected inclusion; (right) 2D Raman spectral image. Different colours show the spatial distribution of the detected phases.

pseudomorphs after melt films and pools (Fig. 3a, b) and in garnet porphyroblasts, such as clusters of inclusions (Fig. 4a). It must to be noted that similar textures in granulite facies rocks have been also interpreted as micro monomineralic veins formed by concentrated NaCl or KCl brines (Perchuk et al., 2000; Harlov, 2012).

Microstructural and microchemical observations confirm the primary origin for both Type I and II inclusions. In particular, their systematic zonal arrangement at the core of garnets is a strong indication of primary entrapment during growth of the peritectic garnet host (Sobolev and Kostyuk, 1975; Roedder, 1979; Cesare et al., 2015). Based on the compositional profiles, Type I and II inclusions mainly occur in the low-Ca portion of the host garnet while they are only occasionally present in the high-Ca annuli (Figs. 11, S3; Table S1). According to the thermodynamic modelling performed by Dumond et al. (2015), the internal portion of the host formed as a consequence of biotite breakdown-melting at 800–900 °C, 0.6–1.0 GPa (Fig. 12), during the prograde loading and burial of these rocks. Assuming that any changes in the host composition have not occurred by retrograde diffusion, we can presume that the inclusions were also entrapped during the formation of the high-Grs annuli at higher temperature and pressure conditions (up to 950 °C and 1.4 GPa). Therefore, Type I multiphase inclusions and nanogranitoids were most likely entrapped at the same P-T conditions and, in turn, during the same first melting event.

The multiphase inclusions hosted in garnet show differences in composition, size and fluid phase occurrence. Inclusions vary from carbon-rich multiphase inclusions (Type I) to less common totally crystallized nanogranitoids (Type II). Because Type I and II inclusions are clearly related to the same melting event (see above), they likely represent different fluids present in the system during anatexis. Type II nanogranitoids are mainly composed of K-feldspar, quartz and plagioclase, with minor amounts of graphite, biotite and aluminosilicate (Fig. 5d–i), suggesting their crystallization from a peraluminous silicate melt (Cesare et al., 2015; Bartoli et al., 2016). Preliminary remelting experiments at 850 °C and 1.5 GPa by piston-cylinder apparatus confirm the occurrence of a granitic melt within Type II inclusions (Table S2).

While type II inclusions can be reliably interpreted as former

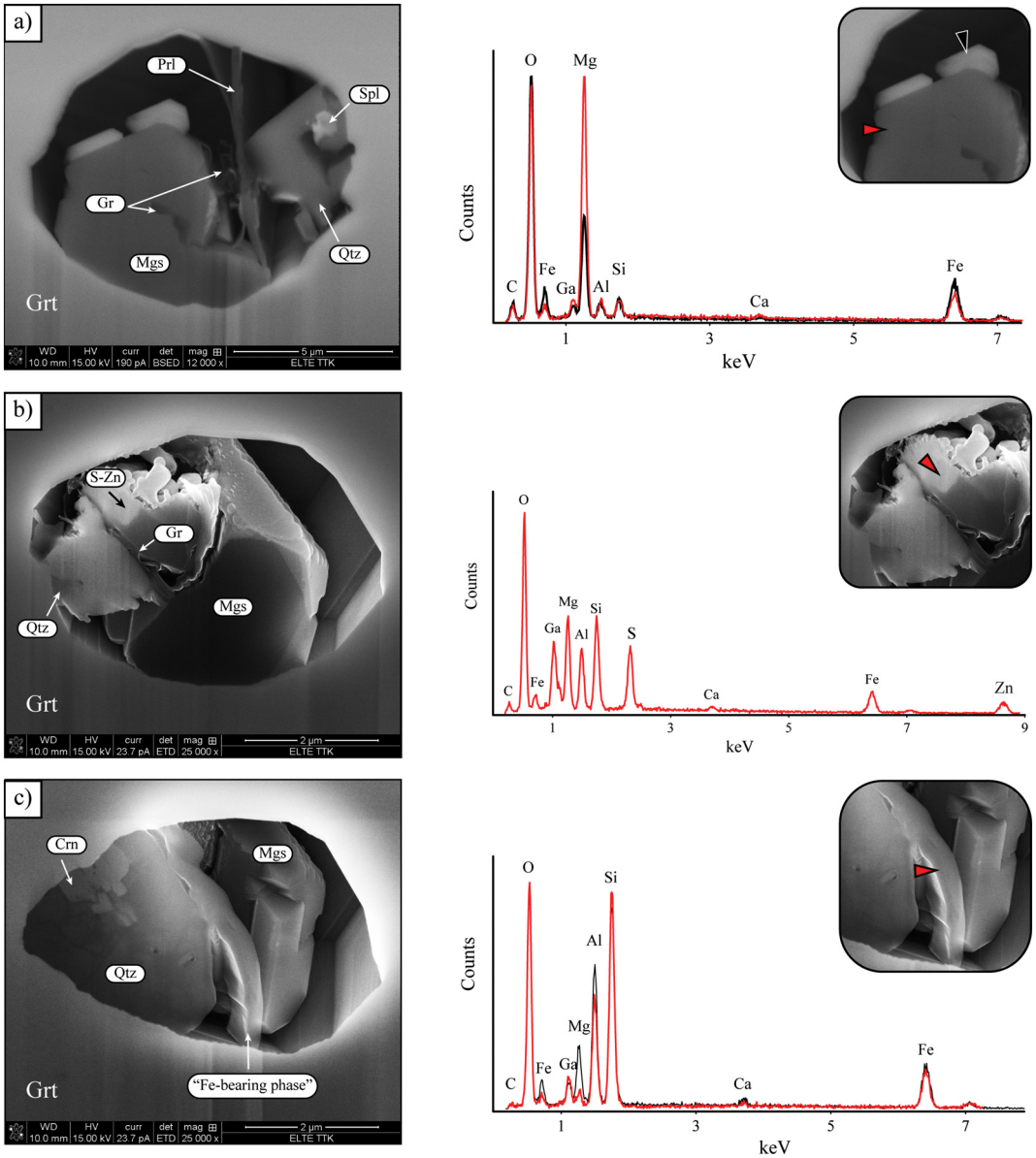

Fig. 8. SE and BSE images and EDS spectra of phases in exposed inclusions by FIB-SEM. Arrows in the close-up views on the right mark the EDS analysis spots. In (c) the host garnet has been also analysed (see the black spectrum in the image on the right).

droplets of silicate crustal melt, inferring the nature and origin of Type I inclusions is less straightforward, as there are no similar examples previously reported or discussed in the literature.

In fact, Type I inclusions are mainly composed of ferroan magnesite (60–80 vol% of solids inside the inclusions), quartz (10–25 vol%) and graphite (< 6.5 vol%). Corundum, Zn-spinel and pyrophyllite are often present while calcite and dolomite are less common (Table 2). These inclusions are smaller in size (≤15 μm) than nanogranitoids (≤50 μm) and they contain a CO_2-rich fluid with traces of N_2 and CH_4 (Fig. 6c). The composition of ferroan magnesite within the solid solution between magnesite and siderite has been confirmed both by Raman microspectroscopy and FIB-SEM observations (Figs. 6a, 8a). In particular, it has been shown that Fe^{2+}-Mg^{2+} substitution results in an evident shift of the characteristic Raman peaks in the region between 100 and 300 cm^{-1} (Boulard et al., 2011). According to the method proposed by Boulard et al. (2011) and on the basis of the collected spectra, the estimated Fe# value [Fe# = 100*Fe/(Fe + Mg + Mn + Ca + Al)] generally varies between 20 (based on bands at 1094, 320 and 207 cm^{-1}) and 35 (based on bands at 1091, 312 and 200 cm^{-1}) within the magnesite. Calcite and dolomites occurrences, often associated to magnesite, could be the result of local enrichment in Ca and Mg promoting the crystallization of different carbonates.

The ubiquitous presence of carbonates, graphite and CO_2 within Type I inclusions clearly suggest the entrapment of a carbon-rich fluid. Moreover, considering the fairly constant mineral assemblage and similar relative volume proportions of ferroan magnesite, quartz and graphite (Table 2), the entrapped fluid was likely homogeneous in composition (see below).

The coexistence of two types of inclusion showing different nature and composition can be explained by an immiscibility process (unmixing of melts and/or fluids). This phenomenon is well-documented in magmatic systems and several types of magmatic immiscibility have been described (see Kamenetsky, 2006; Audetat and Lowenstern, 2014; and references therein). In contrast, fluid-melt or fluid-melt-melt immiscibility has been rarely reported in anatectic rocks (Cesare et al., 2007; Ferrero et al., 2011, 2016b).

As a first hypothesis, given their high proportions of carbonates (60–80 vol%), Type I multiphase inclusions could represent the

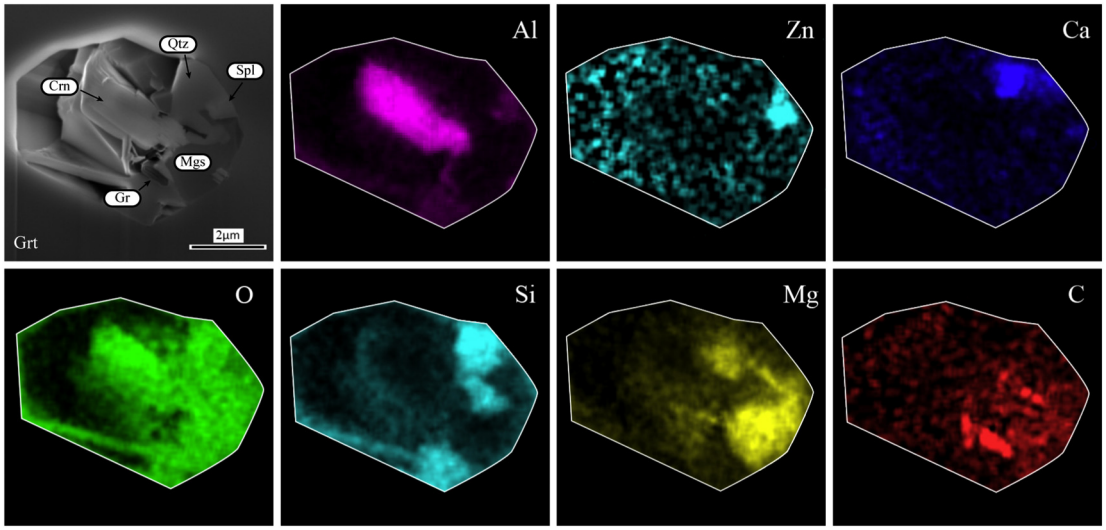

Fig. 9. SE image (image at upper left corner) and EDS X-rays element distribution maps for Al, Zn, Ca, O, Si, Mg and C of a Type I multiphase inclusion. Element distribution support the identification of phases based on Raman analyses. Note that Ca distribution is due to a dolomite crystal few nanometers below quartz.

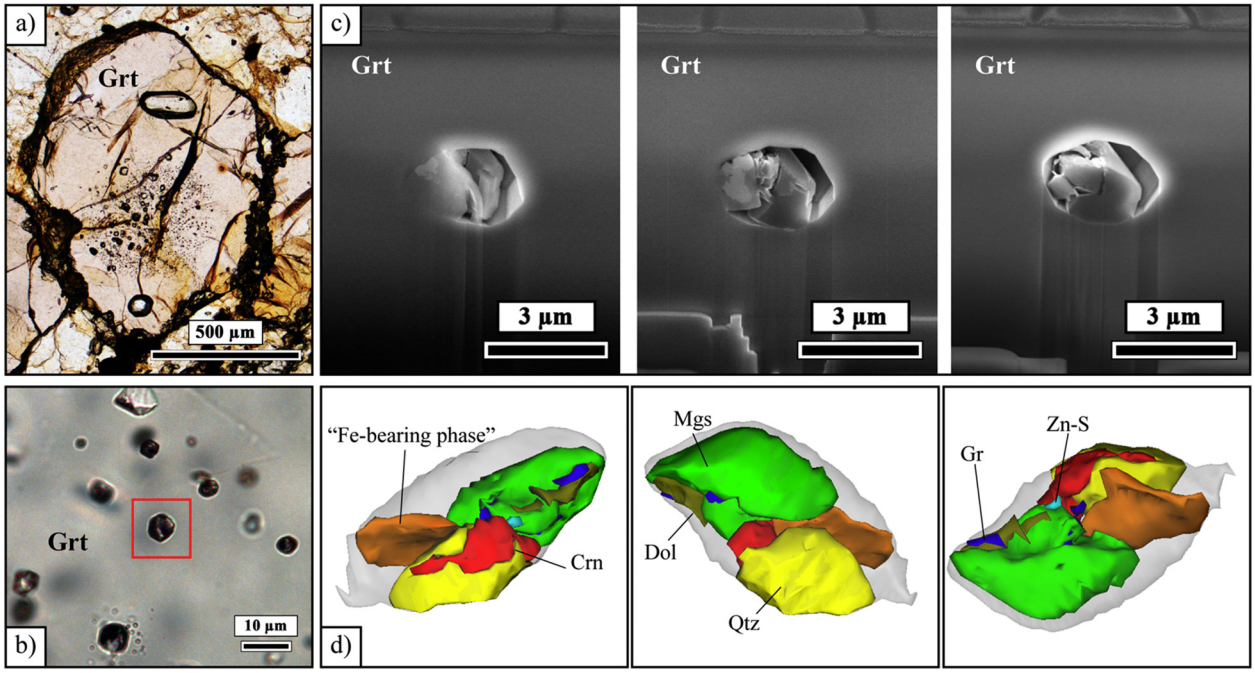

Fig. 10. 3D reconstruction of one of the analysed inclusions obtained by stepwise sectioning using FIB-SEM. (a) Plane-polarized light photomicrograph of a garnet porphyroblast. Clusters of multiphase inclusions are visible at the core of the mineral; (b) close-up view of the analysed inclusion (red square); (c) SE images acquired during the gradual exposure of the selected inclusion; (d) 3D model of the multiphase aggregate filling the analysed inclusion. (For interpretation of the references to colour in this figure legend, the reader is referred to the web version of this article.)

crystallization product of a carbonatitic melt. The coexistence of nanogranitoids and anatectic nanocarbonatites is a recent finding in partially melted crustal rocks. Ferrero et al. (2016b) interpreted the occurrence of calcite, clinochlore and muscovite within some inclusions as the result of entrapment of a carbonatitic melt, and their coexistence with nanogranitoids and COH fluid inclusions as a product of primary immiscibility during anatexis in the lower crust. However, the fluid content in the carbonatitic inclusions of Ferrero et al. (2016b) is much lower than in the studied rocks from the Athabasca granulite terrane where there is no field and petrographic evidence of carbonatitic melt. Therefore, a carbonatitic origin for Type I inclusions appears unlikely.

Alternatively, Type I inclusions could represent original carbonic inclusions that were immiscible with the melt of Type II nanogranitoids (fluid-melt immiscibility). Such immiscibility arises because carbonic fluids are characterized by a very low solubility in silicate melts (Tamic et al., 2001) and easily form CO_2-rich fluid inclusions coexisting with CO_2-saturated melts (Kamenetsky, 2006). Anatectic melt inclusions of rhyolitic composition coexist with immiscible CO_2-rich fluid inclusions in cordierite and garnet in crustal enclaves from El Hoyazo, Spain (Cesare et al., 2007; Ferrero et al., 2014) and in perictectic garnet from the enclaves of La Galite Archipelago, central Mediterranean (Ferrero et al., 2014).

Could Type I inclusions, now occupied for a large part by solids, have initially been fluid inclusions? The formation of step-daughter mineral phases by post-entrapment reactions has been often reported in fluid inclusion studies (Heinrich and Gottschalk, 1995; Kleinefeld and

Table 2
Volumes of each solid phase normalized to the total amount of the solid phases observed in the same inclusion.

	Inclusions						
	1	2	3	4	5	7	8
Solid phase (%)	52%	60%	31%	11%	34%	40%	46%
Phase							
Magnesite	61.7	68.6	66.4	69.5	81.4	59.8	54.7
Quartz	20.5	19.8	11.5	15.7	6.7	25.5	25.8
Graphite	4.9	1.5	1.7	3.2	6.5	1.4	1.0
Corundum	4.6	8.9	n.p.	n.p.	n.p.	9.9	9.3
Zn-spinel	0.2	0.2	2.1	5.7	4.3	2.1	n.p.
Zn-S	n.p	n.p	n.p.	0.7	0.6	0.2	0.2
Calcite	n.p	n.p.	n.p.	0.2	n.p.	n.p.	n.p.
Dolomite	n.p	0.9	n.p.	n.p.	n.p.	n.p.	1.5
Pyrophyllite	5.4	n.p.	n.p.	n.p.	n.p.	n.p.	n.p.
Fe-bearing phase	2.7	n.p.	18.4	5.0	0.5	1.0	7.4
Total	100.0	100.0	100.0	100.0	100.0	100.0	100.0

n.p. = not present.

Bakker, 2002; Frezzotti et al., 2012a; Berkesi et al., 2012; Ferrero et al., 2014; Lamadrid et al., 2014; Frezzotti and Touret, 2014). Considering that carbonates are ubiquitous inside the Type I inclusions but absent in the rock matrix, these multiphase inclusions could represent the product of post-entrapment interaction between former CO_2-rich fluid inclusions and the host garnet. We calculated the P-T location of the equilibrium that represents the model process of fluid-host interaction

garnet + CO_2 = carbonate + kyanite + quartz (1)

using an X_{Mg} of 0.33 for garnet in the FMAS-CO_2 system (Fig. 12). According to reaction (1), Fe-rich garnet may react with CO_2 to form an intermediate magnesite-siderite solution and kyanite during cooling. Therefore, we interpret the presence of ferroan magnesite (with rare calcite and dolomite) in Type I inclusions as a product of post-entrapment interaction between the CO_2-rich fluid and the garnet host during the retrograde path.

Note that, while sillimanite and kyanite are present in the garnet as solid inclusions, they do not occur within Type I inclusions. Instead, corundum and quartz are frequently observed together (Figs. 8c, 9). The association Crn + Qtz is metastable relative to Al_2SiO_5 polymorphs at crustal conditions, but it may be observed in metamorphic rocks due to sluggish kinetics (Harlov et al., 2008). The occurrence of metastable phases is expected in very small multiphase/fluid inclusions (Roedder, 1971). Ferrero et al. (2016a) have recently documented the presence of kumdykolite and kokchetavite, metastable polymorphs of albite and K-feldspar, respectively, in primary nanogranitoid inclusions from granulites of the Bohemian Massif and in the Dronning Maud Land,

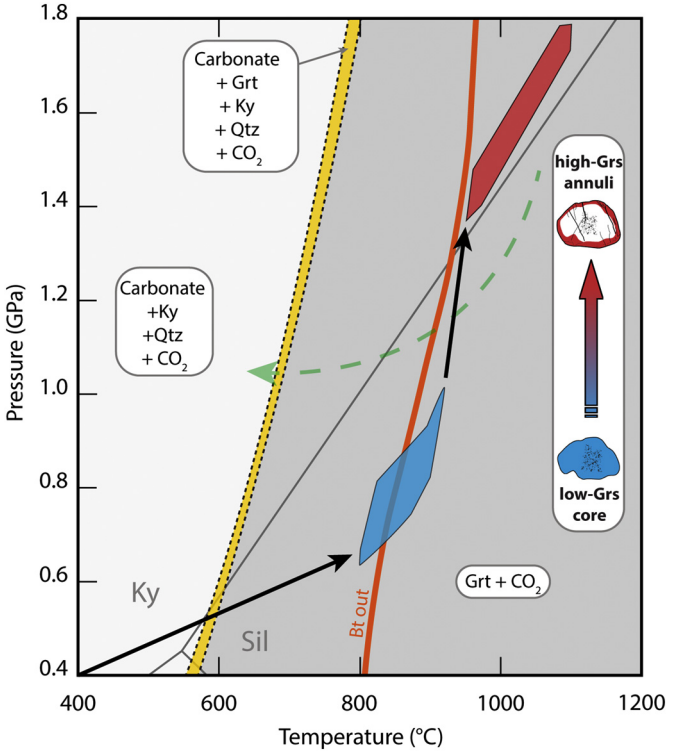

Fig. 12. P-T diagram showing the prograde and retrograde paths for the Upper Deck felsic granulite (slightly modified after Dumond et al., 2015, 2017) compared to the phase equilibria calculated considering a garnet composition with a X_{Mg} = 0.33 (see Table S1) and using the Perple_X 6.7.9 software. The chosen chemical system is FMAS-CO_2. In blue the formation of the low-Grs core (> 800 °C at 0.6–0.8 GPa) where the majority of the Type I and II inclusions occur, while in red the growth of the high-Grs annuli at peak metamorphic conditions (> 1.4 GPa at ≥950 °C). Yellow field indicates the divariant field Carbonate + Grt + Als + Qtz + CO_2. According to these P-T calculations, the trapped CO_2-rich fluid may have reacted with the host garnet during cooling of the rock forming the multiphase assemblage observed in Type I inclusions (see text for details). (For interpretation of the references to colour in this figure legend, the reader is referred to the web version of this article.)

Antarctica (Ferrero et al., 2018). Therefore, on the basis of our observations, we propose a modification of the carbonation reaction (1):

garnet + CO_2 = carbonate + corundum + quartz (2)

which formed the solid assemblage observed in Type I inclusions, and that Crn + Qtz were able to grow metastably due to the very small size

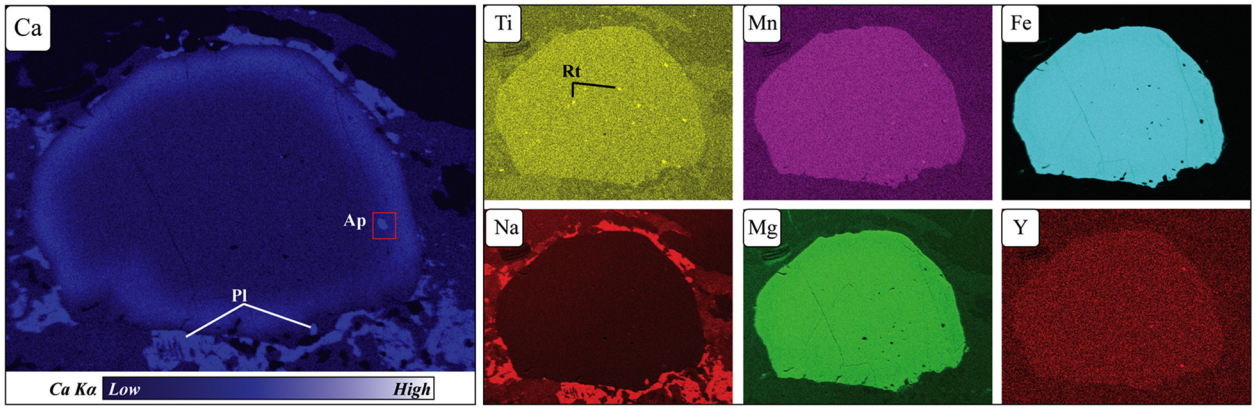

Fig. 11. EDS X-ray element distribution map showing the Ca-zonation of the host garnet. Ca-light blue zones define the high-calcium internal rim of the garnet. Apatite (Ap) and rutile (Rt) are present as inclusion. Plagioclase rims around the garnet are visible. (For interpretation of the references to colour in this figure legend, the reader is referred to the web version of this article.)

of Type I inclusions. The fact that CO_2 is still present in the inclusions despite garnet being in excess may be due to either the divariance of equilibrium or to the slow kinetics at low temperature (Berkesi et al., 2012).

The progress of the carbonation reaction (2) is consistent with the negative correlation between the CO_2 densities and the total amount of solid phases observed within the inclusions (Tables 1, 2). In fact, simultaneous increase of inclusion volume by host consumption, and growth of solids having greater density than fluid must cause a decrease of fluid density, according to the process of closed-system density decrease by step-daughter precipitation modelled by Heinrich and Gottschalk (1995).

Considering that the volume of the inclusions expanded, and the amount of CO_2 decreased, as a result of the model reaction (2), the original density of the entrapped CO_2 fluid has been inferred by restoring the original configuration through consumption of the volumes of carbonate, quartz and corundum obtained from FIB-SEM analyses (see Table 2), i.e., by operating the back-reaction of (2) up to completion, with the calculation of the garnet and CO_2 that would be produced back. Further assumptions of the calculations were that: (i) no fluid leakage occurred after the entrapment; ii) the entrapped fluid was pure CO_2; iii) the X_{Mg} of the carbonate within the inclusions corresponds to the X_{Mg} of the reactant garnet and iv), only carbonate, corundum and quartz were produced by the carbonation reaction. The calculated CO_2 density ranges from 1.5 to 2.2 g/cm^3. These values would define isochores providing a range of trapping pressure of 1.5–2 GPa, at the trapping temperature of 800–900 °C. The estimated pressures are in general higher than those predicted by phase equilibria modelling (up to 1.4 GPa; Fig. 12). Considering the robust petrologic constrain (in terms of inclusion microstructures and P-T estimates), this discrepancy is likely related to the aforementioned simplifications and assumptions in performing the mass balance calculations. It should be noted, however, that the lower density (ca. 1.5 g/cm^3) is consistent with conditions of entrapment of > 850 °C and ≥ 1.4 GPa.

The common finding of small amounts of daughter pyrophyllite and graphite within Type I inclusions, suggests reaction (2) should be considered a first approximation model to the actual process that took place, as some amount of H_2O and excess carbon must also have been present in the original fluid. Pyrophyllite represents the hydrated counterpart of an Al_2SiO_5 + Qtz (or Crn + Qtz) assemblage such as the one predicted or observed in the inclusions. Detailed Raman study did not find evidence of H_2O within Type I inclusions, nor of hydro-garnet at inclusion/host interface (Kolesov and Geiger, 2005; Lamadrid et al., 2014). The lack of clear evidence of H_2O in Type I inclusions is difficult to reconcile with the hydrous character of coexisting Type II melts, inferred from the low EMP totals of remelted nanogranites (Table S2).

With the available data we can speculate that the H_2O component may have been totally consumed by pyrophyllite growth, and/or lost along decrepitation nanocracks, not visible by optical microscope and SEM. For example, Ferrero et al. (2011) documented, by means of TEM, the occurrence of cracks at the nanoscale connected to fluid inclusions.

Concerning carbon in Type I inclusions, this element is stored essentially in the CO_2 fluid component and in carbonate, and secondary by CH_4 and graphite. The carbonic fluids originally trapped as fluid inclusions and subsequently modified into Type I multiphase inclusions probably have an internal origin (i.e., produced in a closed system). In fact, given the presence of graphite in the rock matrix surrounding garnet, graphite-saturated carbonic fluids can be generated in a closed-system scenario either by subsolidus devolatilization (Connolly and Cesare, 1993) or by suprasolidus fluid-absent melting of Fe^{3+}-bearing biotite (Cesare et al., 2005). In both cases, these fluids can become CO_2-rich during re-speciation upon cooling (Cesare et al., 2005).

The alternative possibility of infiltration of carbonic fluids from an external source cannot be ruled out. In the studied rocks, CO_2 could have been released by intraplating mafic magmas which have facilitated the partial melting of the protolith during the Neoarchean at 2.61–2.55 Ga (Dumond et al., 2015, 2017).

8. Conclusions

Peritectic garnet of the felsic granulite from the Upper Deck domain (Athabasca granulite terrane, Canada) contains primary CO_2-rich multiphase inclusions (Type I) and nanogranitoids (Type II). Type I multiphase inclusions are abundant and mainly composed of ferroan magnesite, quartz and graphite. In addition to the solid phases, these inclusions contain a CO_2-rich fluid with traces of N_2 and CH_4. Type I inclusions coexist with nanogranitoids (mainly composed of K-feldspar, quartz and plagioclase with minor biotite and aluminosilicate), representing former droplets of anatectic silicate melt. Type I and II multiphase inclusions are related to the same partial melting event and were trapped at 800–950 °C during progressive burial from 0.6 up to 1.4 GPa. Differences in the nature and composition between Type I and II inclusions indicate a situation of melt-fluid immiscibility during anatexis, with coexistence of a carbon-rich fluid and silicate melt. Detailed microstructural and microchemical characterization along with phase equilibria modelling indicate that most of the solid phases within Type I inclusions are related to a post-entrapment carbonation reaction between the host garnet and original CO_2-bearing fluid during cooling of the rock. This contribution clearly shows evidence of carbon mobility during the Neoarchean anatexis of this portion of the lower continental crust.

Supplementary data to this article can be found online at https://doi.org/10.1016/j.chemgeo.2018.05.043.

Acknowledgements

This research benefitted from funding from the Italian Ministry of Education, University, Research (Grant SIR RBSI14Y7PF to O.B.). This work was supported by the Bolyai Postdoctoral Fellowship Program grant awarded to M. Berkesi. The authors thank J. L. R. Touret and S. Ferrero for their reviews of the manuscript and K. Mezger for the editorial handling. J. A. D. Connolly is also acknowledged for his suggestions during phase equilibria modelling. The authors owe thanks to A. Német, G. Varga and Á. Szabó (Eötvös University, Hungary) for assistance during the FIB-SEM analyses and to M. Crivellaro (University of Padova, Italy) for helpful discussions.

References

Acosta-Vigil, A., Cesare, B., London, D., Morgan, G.B.V.I., 2007. Microstructures and composition of melt inclusions in a crustal anatectic environment, represented by metapelitic enclaves within El Hoyazo dacites, SE Spain. Chem. Geol. 235, 450–465.

Acosta-Vigil, A., Buick, I., Hermann, J., Cesare, B., Rubatto, D., London, D., Morgan VI, G.B., 2010. Mechanisms of crustal anatexis: a geochemical study of partially melted metapelitic enclaves and host dacite, SE Spain. J. Petrol. 51, 785–821.

Audetat, A., Lowenstern, J.B., 2014. Melt inclusions. In: Holland, H.D., Turekian, K.K. (Eds.), Treatise on Geochemistry, Second edition. Elsevier, Oxford, pp. 143–173.

Baldwin, J.A., Bowring, S.A., Williams, M.L., 2003. Petrological and geochronological constraints on high pressure, high temperature metamorphism in the snowbird tectonic zone, Canada. J. Metamorph. Geol. 21, 81–98.

Baldwin, J.A., Williams, M.L., Williams, I.S., Bowring, S.A., 2004. Eclogites of the snowbird tectonic zone: petrological and U-Pb geochronological evidence for Paleoproterozoic high-pressure metamorphism in the western Canadian shield. Contrib. Mineral. Petrol. 147, 528–548.

Baldwin, J.A., Bowring, S.A., Williams, M.L., Mahan, K.H., 2006. Geochronological constraints on the evolution of high-pressure felsic granulites from an integrated electron microprobe and ID-TIMS geochemical study. Lithos 88, 173–200. http://dx.doi.org/10.1016/j.lithos.2005.08.009.

Baldwin, J.A., Powell, R., Williams, M.L., Goncalves, P., 2007. Formation of eclogite, and reaction during exhumation to mid-crustal levels, Snowbird tectonic zone, western Canadian shield. J. Metamorph. Geol. 25, 953–974.

Baldwin, J.A., Powell, R., White, R.W., Štípská, P., 2015. Using calculated chemical potential relationships to account for replacement of kyanite by symplectite in high pressure granulites. J. Metamorph. Geol. 33, 311–330. http://dx.doi.org/10.1111/jmg.12122.

Bartoli, O., Cesare, B., Poli, S., Bodnar, R.J., Acosta-Vigil, A., Frezzotti, M.L., Meli, S., 2013a. Recovering the composition of melt and the fluid regime at the onset of crustal anatexis and S-type granite formation. Geology 41, 115–118.

Bartoli, O., Cesare, B., Poli, S., Acosta-Vigil, A., Esposito, R., Turina, A., Bodnar, R.J., Angel, R.J., Hunter, J., 2013b. Nanogranite inclusions in migmatitic garnet: behavior during piston-cylinder remelting experiments. Geofluids 13, 405–420. http://dx.doi.org/10.1111/gfl.12038.

Bartoli, O., Cesare, B., Remusat, L., Acosta-Vigil, A., Poli, S., 2014. The H_2O content of granite embryos. Earth Planet. Sci. Lett. 395, 281–290. http://dx.doi.org/10.1016/j.epsl.2014.03.031.

Bartoli, O., Acosta-Vigil, A., Ferrero, S., Cesare, B., 2016. Granitoid magmas preserved as melt inclusions in high-grade metamorphic rock. Am. Mineral. 101, 1543–1559. http://dx.doi.org/10.2138/am-2016-5541CCBYNCND.

Berkesi, M., Hidas, K., Guzmics, T., Dubessy, J., Bodnar, R.J., Szabó, C., Vajna, B., Tsunogae, T., 2009. Detection of small amounts of H_2O in CO_2 -rich fluid inclusions using Raman spectroscopy: detection of H_2O in CO_2 -rich fluid inclusions using Raman spectroscopy. J. Raman Spectrosc. 40, 1461–1463. http://dx.doi.org/10.1002/jrs.2440.

Berkesi, M., Guzmics, T., Szabó, C., Dubessy, J., Bodnar, R.J., Hidas, K., Ratter, K., 2012. The role of CO_2-rich fluids in trace element transport and metasomatism in the lithospheric mantle beneath the central Pannonian Basin, Hungary, based on fluid inclusions in mantle xenoliths. Earth Planet. Sci. Lett. 331–332, 8–20. http://dx.doi.org/10.1016/j.epsl.2012.03.012.

Berkesi, M., Káldos, R., Park, M., Szabó, C., Váczi, T., Török, K., Németh, B., Czuppon, G., 2017. Detection of small amounts of N_2 in CO_2 -rich high-density fluid inclusions from mantle xenoliths. Eur. J. Mineral. 29, 423–431. http://dx.doi.org/10.1127/ejm/2017/0029-2615.

Boulard, E., Guyot, F., Fiquet, G., 2011. The influence on Fe content on Raman spectra and unit cell parameters of magnesite–siderite solid solutions. Phys. Chem. Miner. 39, 239–246. http://dx.doi.org/10.1007/s00269-011-0479-3.

Brown, M., 2006. Melt extraction from the lower continental crust of orogens: the field evidence. In: Brown, M., Rushmer, T. (Eds.), Evolution and Differentiation of the Continental Crust. Cambridge University Press, Cambridge, UK, pp. 332–384.

Brown, M., 2007. Crustal melting and melt extraction, ascent and emplacement in orogens: mechanisms and consequences. J. Geol. Soc. 164, 709–730.

Brown, M., 2013. Granite: from genesis to emplacement. Geol. Soc. Am. Bull. 125, 1079–1113.

Cesare, B., Maineri, C., 1999. Fluid-present anatexis of metapelites at El Joyazo (SE Spain): constraints from Raman spectroscopy of graphite. Contrib. Mineral. Petrol. 135, 41–52.

Cesare, B., Meli, S., Nodari, L., Russo, U., 2005. Fe^{3+} reduction during biotite melting in graphitic metapelites: another origin of CO_2 in granulites. Contrib. Mineral. Petrol. 149, 129–140. http://dx.doi.org/10.1007/s00410-004-0646-3.

Cesare, B., Maineri, C., Baron Toaldo, A., Pedron, D., Acosta Vigil, A., 2007. Immiscibility between carbonic fluids and granitic melts during crustal anatexis: a fluid and melt inclusion study in the enclaves of the Neogene Volcanic Province of SE Spain. Chem. Geol. 237, 433–449. http://dx.doi.org/10.1016/j.chemgeo.2006.07.013.

Cesare, B., Ferrero, S., Salvioli-Mariani, E., Pedron, D., Cavallo, A., 2009. Nanogranite and glassy inclusions: the anatectic melt in migmatites and granulites. Geology 37, 627–630.

Cesare, B., Acosta-Vigil, A., Ferrero, S., Bartoli, O., 2011. Melt inclusions in migmatites and granulites. J. Virtual Explor. 38. http://dx.doi.org/10.3809/jvirtex.2011.00268.

Cesare, B., Acosta-Vigil, A., Bartoli, O., Ferrero, S., 2015. What can we learn from melt inclusions in migmatites and granulites? Lithos 239, 186–216. http://dx.doi.org/10.1016/j.lithos.2015.09.028.

Connolly, J.A.D., Cesare, B., 1993. C-0-H-S fluid composition and oxygen fugacity in graphitic metapelites. J. Metamorph. Geol. 11, 379–388.

Dubessy, J., Poty, B., Ramboz, C., 1989. Advances in C-O-H-N-S fluid geochemistry based on micro-Raman spectrometric analysis of fluid inclusions. Eur. J. Mineral. 1, 517–534.

Dumond, G., McLean, N., Williams, M.L., Jercinovic, M.J., Bowring, S.A., 2008. High-resolution dating of granite petrogenesis and deformation in a lower crustal shear zone: Athabasca granulite terrane, western Canadian shield. Chem. Geol. 254, 175–196. http://dx.doi.org/10.1016/j.chemgeo.2008.04.014.

Dumond, G., Goncalves, P., Williams, M.L., Jercinovic, M.J., 2010. Subhorizontal fabric in exhumed continental lower crust and implications for lower crustal flow: Athabasca granulite terrane, western Canadian Shield. Tectonics 29 (n/a–n/a). https://doi.org/10.1029/2009TC002514.

Dumond, G., Mahan, K.H., Williams, M.L., Jercinovic, M.J., 2013. Transpressive uplift and exhumation of continental lower crust revealed by synkinematic monazite reactions. Lithosphere 5, 507–512. http://dx.doi.org/10.1130/L292.1.

Dumond, G., Goncalves, P., Williams, M.L., Jercinovic, M.J., 2015. Monazite as a monitor of melting, garnet growth and feldspar recrystallization in continental lower crust. J. Metamorph. Geol. 33, 735–762. http://dx.doi.org/10.1111/jmg.12150.

Dumond, G., Williams, M.L., Baldwin, J.A., Jercinovic, M.J., 2017. Backarc origin for Neoarchean ultrahigh-temperature metamorphism, eclogitization, and orogenic root growth. Geology 45, 943–946. http://dx.doi.org/10.1130/G39254.1.

Farina, F., Albert, C., Lana, C., 2015. The Neoarchean transition between medium- and high-K granitoids: clues from the southern São Francisco craton (Brazil). Precambrian Res. 266, 375–394. http://dx.doi.org/10.1016/j.precamres.2015.05.038.

Ferrero, S., Bodnar, R.J., Cesare, B., Viti, C., 2011. Re-equilibration of primary fluid inclusions in peritectic garnet from metapelitic enclaves, El Hoyazo, Spain. Lithos 124, 117–131. http://dx.doi.org/10.1016/j.lithos.2010.09.004.

Ferrero, S., Bartoli, O., Cesare, B., Salvioli-Mariani, E., Acosta-Vigil, A., Cavallo, A., Groppo, C., Battiston, S., 2012. Microstructures of melt inclusions in anatectic metasedimentary rocks. J. Metamorph. Geol. 30, 303–322. http://dx.doi.org/10.1111/j.1525-1314.2011.00968.x.

Ferrero, S., Braga, R., Berkesi, M., Cesare, B., Laridhi Ouazaa, N., 2014. Production of metaluminous melt during fluid-present anatexis: an example from the Maghrebian basement, La Galite archipelago, Central Mediterranean. J. Metamorph. Geol. 32, 209–225. http://dx.doi.org/10.1111/jmg.12068.

Ferrero, S., Ziemann, M.A., Angel, R.J., O'Brien, P.J., Wunder, B., 2016a. Kumdykolite, kokchetavite, and cristobalite crystallized in nanogranites from felsic granulites, Orlica-Snieznik dome (Bohemian Massif): not evidence for ultrahigh-pressure conditions. Contrib. Mineral. Petrol. 171. http://dx.doi.org/10.1007/s00410-015-1220-x.

Ferrero, S., Wunder, B., Ziemann, M.A., Wälle, M., O'Brien, P.J., 2016b. Carbonatitic and granitic melts produced under conditions of primary immiscibility during anatexis in the lower crust. Earth Planet. Sci. Lett. 454, 121–131. http://dx.doi.org/10.1016/j.epsl.2016.08.043.

Ferrero, S., Godard, G., Palmeri, R., Wunder, B., Cesare, B., 2018. Partial melting of ultramafic granulites from Dronning Maud land, Antarctica: constraints from melt inclusions and thermodynamic modeling. Am. Mineral. 103, 610–622. http://dx.doi.org/10.2138/am-2018-6214.

Flowers, R.M., Bowring, S.A., Williams, M.L., 2006. Timescales and significance of high-pressure, high-temperature metamorphism and mafic dike anatexis, Snowbird tectonic zone, Canada. Contrib. Mineral. Petrol. 151, 558–581.

Frezzotti, M.L., Touret, J.L.R., 2014. CO_2, carbonate-rich melts, and brines in the mantle. Geosci. Front. 5, 697–710. http://dx.doi.org/10.1016/j.gsf.2014.03.014.

Frezzotti, M.L., Ferrando, S., Tecce, F., Castelli, D., 2012a. Water content and nature of solutes in shallow-mantle fluids from fluid inclusions. Earth Planet. Sci. Lett. 351–352, 70–83. http://dx.doi.org/10.1016/j.epsl.2012.07.023.

Frezzotti, M.L., Tecce, F., Casagli, A., 2012b. Raman spectroscopy for fluid inclusion analysis. J. Geochem. Explor. 112, 1–20. http://dx.doi.org/10.1016/j.gexplo.2011.09.009.

Hanmer, S., 1994. Geology, East Athabasca Mylonite Triangle, Saskatchewan: Map 1859A, Scale 1:100000. Geological Survey of Canada, Ottawa.

Hanmer, S., 1997. Geology of the Striding Athabasca mylonite zone, northern Saskatchewan and southeastern District of Mackenzie, Northwest Territories, Bulletin/Geological Survey of Canada. Her Majesty the Queen in Right of Canada, Ottawa.

Hanmer, S., Parrish, R., Williams, M., Kopf, C., 1994. Striding-Athabasca mylonite zone: complex Archean deep-crustal deformation in the East Athabasca mylonite triangle, northern Saskatchewan. Can. J. Earth Sci. 31, 1287–1300. http://dx.doi.org/10.1139/e94-111.

Hanmer, S., Williams, M., Kopf, C., 1995a. Striding-Athabasca mylonite zone: implications for the Archean and Early Proterozoic tectonics of the western Canadian shield. Can. J. Earth Sci. 32, 178–196.

Hanmer, Williams, M.L., Kopf, C., 1995b. Modest movements, spectacular fabrics in an intracontinental deep-crustal strike-slip fault: striding-Athabasca mylonite zone, NW Canadian Shield. J. Struct. Geol. 17, 493–507.

Harlov, D.E., 2012. The potential role of fluids during regional granulite-facies dehydration in the lower crust. Geosci. Front. 3, 813–827. http://dx.doi.org/10.1016/j.gsf.2012.03.007.

Harlov, D.E., Milke, R., Gottschalk, M., 2008. Metastability of sillimanite relative to corundum and quartz in the kyanite stability field: competition between stable and metastable reactions. Am. Mineral. 93, 608–617. http://dx.doi.org/10.2138/am.2008.2655.

Heinrich, W., Gottschalk, M., 1995. Metamorphic reactions between fluid inclusions and mineral hosts. I. Progress of the reaction calcite + quartz = wollastonite + CO_2 in natural wollastonite-hosted fluid inclusions. Contrib. Mineral. Petrol. 122, 51–61.

Hollister, L.S., 1988. On the origin of CO_2-rich fluid inclusions in migmatites. J. Metamorph. Geol. 6, 467–474.

Holness, M.B., Sawyer, E.W., 2008. On the pseudomorphing of melt-filled pores during the crystallization of Migmatites. J. Petrol. 49, 1343–1363. http://dx.doi.org/10.1093/petrology/egn028.

Holness, M.B., Cesare, B., Sawyer, E.W., 2011. Melted rocks under the microscope: microstructures and their interpretation. Elements 7, 247–252. http://dx.doi.org/10.2113/gselements.7.4.247.

Jamieson, R.A., Unsworth, M.J., Harris, N.B.W., Rosenberg, C.L., Schulmann, K., 2011. Crustal melting and the flow of mountains. Elements 7, 253–260. http://dx.doi.org/10.2113/gselements.7.4.253.

Kamenetsky, V.S., 2006. Melt inclusion record of magmatic immiscibility in crustal and mantle magmas. Melt Incl. Plutonic Rocks 81–98.

Kleinefeld, B., Bakker, R.J., 2002. Fluid inclusions as microchemical systems: evidence and modelling of fluid–host interactions in plagioclase. J. Metamorph. Geol. 20, 845–858.

Kolesov, B.A., Geiger, C.A., 2005. The vibrational spectrum of synthetic hydrogrossular (katoite) $Ca_3Al_2(O_4H_4)_3$: a low-temperature IR and Raman spectroscopic study. Am. Mineral. 90, 1335–1341.

Kopf, C., 1999. Deformation, Metamorphism, and Magmatism in the East Athabasca Mylonite Triangle, Northern Saskatchewan: Implications for the Archean and Early Proterozoic Crustal Structure of the Canadian Shield. PhD Dissertation. University of Massachusetts-Amherst, Amherst, MA.

Kretz, R., 1983. Symbols for rock-forming minerals. Am. Mineral. 68, 277–279.

Lafuente, B., Downs, R.T., Yang, H., Stone, N., 2015. The power of databases: the RRUFF project. In: Armbruster, T., Danisi, R.M. (Eds.), Highlights in Mineralogical Crystallography. W. De Gruyter, Berlin, Germany, pp. 1–30.

Lamadrid, H.M., Lamb, W.M., Santosh, M., Bodnar, R.J., 2014. Raman spectroscopic characterization of H_2O in CO_2-rich fluid inclusions in granulite facies metamorphic rocks. Gondwana Res. 26, 301–310. http://dx.doi.org/10.1016/j.gr.2013.07.003.

Laurent, O., Martin, H., Moyen, J.F., Doucelance, R., 2014. The diversity and evolution of late-Archean granitoids: evidence for the onset of "modern-style" plate tectonics between 3.0 and 2.5Ga. Lithos 205, 208–235. http://dx.doi.org/10.1016/j.lithos.2014.06.012.

Mahan, K.H., Williams, M.L., 2005. Reconstruction of a large deep-crustal terrane: implications for the snowbird tectonic zone and early growth of Laurentia. Geology 33, 385–388.
Mahan, K.H., Williams, M.L., Baldwin, J.A., 2003. Contractional uplift of deep crustal rocks along the Legs Lake shear zone, western Churcill Province, Canadian shield. Can. J. Earth Sci. 40, 1085–1110.
Mahan, K.H., Goncalves, P., Williams, M.L., Jercinovic, M.J., 2006. Dating metamorphic reactions and fluid flow: application to exhumation of high-P granulites in a crustalscale shear zone, western Canadian shield. J. Metamorph. Geol. 24, 193–217.
Mahan, K.H., Goncalves, P., Flowers, R., Williams, M.L., Hoffman-Setka, D., 2008. The role of heterogeneous strain in the development and preservation of a polymetamorphic record in high- *P* granulites, western Canadian shield. J. Metamorph. Geol. 26, 669–694. http://dx.doi.org/10.1111/j.1525-1314.2008.00783.x.
Mahan, K.H., Smit, C.A., Williams, M.L., Dumond, G., van Reenen, D.D., 2011. Heterogeneous strain and polymetamorphism in high-grade terranes: insight into crustal processes from the Athabasca Granulite Terrane, western Canada, and the Limpopo complex, southern Africa. In: van Reenen, D.D., Kramers, J.D., McCourt, S., Perchuk, L.L. (Eds.), Origin and Evolution of High-grade Gneiss Terranes, with Special Emphasis on the Limpopo Complex of Southern Africa. 207. pp. 269–287 Geological Society of America Memoir.
Newton, R.C., 1980. Carbonic metamorphism, granulites and crustal growth. Nature 288, 45–50.
Perchuk, L.L., Safonov, O.G., Gerya, T.V., Fu, B., Harlov, D.E., 2000. Mobility of components in metasomatic transformation and partial melting of gneisses: an example from Sri Lanka. Contrib. Mineral. Petrol. 140, 212–232.
Regan, S.P., Williams, M.L., Leslie, S., Mahan, K.H., Jercinovic, M.J., Holland, M.E., Gibson, D., 2014. The Cora Lake shear zone, Athabasca granulite terrane, an intraplate response to far-field orogenic processes during the amalgamation of Laurentia. Can. J. Earth Sci. 51, 877–901. http://dx.doi.org/10.1139/cjes-2014-0015.
Roedder, E., 1971. Composition of fluid inclusions. US Geol. Surv. Prof. Pap. 164 440JJ.
Roedder, E., 1979. Fluid Inclusions as Samples of Ore Fluids. In: Barnes, H.L. (Ed.), Geochemistry of Hydrothermal Ore Deposits, 2nd ed. Wiley, New York, pp. 684–737.
Roedder, E., 1984. Fluid inclusions. Mineralogical Society of America. Rev. Mineral. 12.
Santosh, M., Tsunogae, T., Ohyama, H., Sato, K., Li, J.H., Liu, S.J., 2008. Carbonic metamorphism at ultrahigh-temperatures: evidence from North China craton. Earth Planet. Sci. Lett. 266, 149–165. http://dx.doi.org/10.1016/j.epsl.2007.10.058.
Sawyer, E.W., Cesare, B., Brown, M., 2011. When the continental crust melts. Elements 7, 229–234. http://dx.doi.org/10.2113/gselements.7.4.229.
Snoeyenbos, D.R., Williams, M.L., Hanmer, S., 1995. Archean high-pressure metamorphism in the western Canadian shield. Eur. J. Mineral. 7, 1251–1272. http://dx.doi.org/10.1127/ejm/7/6/1251.
Sobolev, V.S., Kostyuk, V.P., 1975. Magmatic crystallization based on a study of melt inclusions. Fluid Incl. Res. 9, 182–253.
Spencer, C.J., Roberts, N.M.W., Santosh, M., 2017. Growth, destruction, and preservation of Earth's continental crust. Earth-Sci. Rev. 172, 87–106. http://dx.doi.org/10.1016/j.earscirev.2017.07.013.
Tamic, N., Behrens, H., Holtz, F., 2001. The solubility of H_2O and CO_2 in rhyolitic melts in equilibrium with a mixed CO_2–H_2O fluid phase. Chem. Geol. 174, 333–347.
Touret, J., Dietvorst, P., 1983. Fluid inclusions in high-grade anatectic metamorphites. J. Geol. Soc. 140, 635–649.
Wang, X., Chou, I.-M., Hu, W., Burruss, R.C., Sun, Q., Song, Y., 2011. Raman spectroscopic measurements of CO_2 density: experimental calibration with high-pressure optical cell (HPOC) and fused silica capillary capsule (FSCC) with application to fluid inclusion observations. Geochim. Cosmochim. Acta 75, 4080–4093. http://dx.doi.org/10.1016/j.gca.2011.04.028.
Weinberg, R.F., Hasalová, P., 2015. Water-fluxed melting of the continental crust: a review. Lithos 212–215, 158–188. http://dx.doi.org/10.1016/j.lithos.2014.08.021.
Williams, M.L., Hanmer, S., 2006. Structural and metamorphic processes in the lower crust: evidence from a deep-crustal isobarically cooled terrane, Canada. In: Brown, M., Rushmer, T. (Eds.), Evolution and Differentiation of the Continental Crust. Cambridge University Press, Cambridge, pp. 231–267.
Williams, M.L., Kopf, C., Hanmer, S., Melis, E.A., 2000. Microstructural tectonometamorphic processes and the development of gneissic layering: a mechanism for metamorphic segregation. J. Metamorph. Geol. 18, 41–57.
Williams, M.L., Karlstrom, K.E., Dumond, G., Mahan, K.H., 2009. Perspectives on the architecture of continental crust from integrated field studies of exposed isobaric sections. Geol. Soc. Am. Spec. Pap. 456, 219–241.
Wopenka, B., Pasteris, J.D., 1993. Structural characterization of kerogens to granulite-facies graphite: applicability of Raman microprobe spectroscopy. Am. Mineral. 78, 533–557.